Physical Resistance Components of a Hydrofoil as a Function of Submergence

L Chernyshev[a*], Dr. N Kabaliuk[a], Prof M Jermy[a], Dr. S Corkery[b], Dr. D Bernasconi[b]

[a]*University of Canterbury, New Zealand;* [b]*Emirates Team New Zealand, New Zealand*
[*]Corresponding author. Email: lev.chernyshev@pg.canterbury.ac.nz

Synopsis

Hydrofoils have become a popular design addition to different kinds of vessels, particularly yachts and race boats. Predicting hydrodynamic forces acting on hydrofoils remains challenging, due to a wide operating regime and complex hydrodynamical phenomena. In this paper we investigate methods of decomposing the total drag force of a hydrofoil from high-fidelity Reynolds–Averaged Navier Stokes (RANS) and low-fidelity lifting line computational fluid dynamics simulations into its physical components. Namely, these are the wave-pattern, induced, and viscous drag components. These components were calculated using wake surveys in RANS, while a separation of downwash coefficients was used in the lifting line formulation. Reynolds numbers between 2.57×10^5 and 2.06×10^6 were simulated, which corresponded to chord Froude numbers between 0.5 and 4. We present various Froude number-dependent trends in these components which we observed from RANS. Lifting-line models were modified to account for free surface effects using a mirror image of the hydrofoil as well as free surface Green's function for the wave pattern; and benchmarked against RANS results to gauge their accuracy. A parameter study of submergence depth was also carried out using the lifting line model. Strong submergence-dependence of the induced and wave drag components was observed. Higher submergences led to overall lower total drag except at Froude numbers below around 1.5. In this intermediate regime, strong wave effects acted to increase the total drag compared to even shallower submergences. The efficiency of the numerical LL model here, demonstrated through an extensive parameter study on submergence depth, can be greatly exploited for exploring a large design space to optimise candidate designs during preliminary conception. However, great care should be taken in interpreting these results as the theoretical models employed, especially for the free surface effects, can be difficult to validate and still shows significant discrepancies with CFD.

Keywords: Hydrofoil, computational fluid dynamics, lifting-line, resistance, waves.

1 Introduction

Hydrofoil-equipped craft have become popular in many fields of yachting and boating. In yacht racing, their adoption became widespread after Emirates Team New Zealand introduced them as a design element for their 2013 America's Cup campaign. There are a myriad of other race classes that also incorporate hydrofoils (henceforth "foils") such as the IMOCA60, Waszp, and Olympic Nacra 17. In such cases, foil design is dictated by the class rules - a set of technical regulations that impose geometrical, structural and/or hydrodynamic restrictions on design. Aside from racing, foiling craft find uses in recreational and general-use boating and sailing: on superyachts, sport boats, multihulls, passenger ferries, and others. Here their design is less constrained and has more scope. The use of foils on watercraft adds substantial design complexity and challenge that requires significant effort from designers to overcome.

The use of foils on watercraft may serve different purposes depending on the application. On some craft, foils are used principally to provide an enhanced righting moment to permit greater sail power (Oliver and Gauvain, 2022). On others, the vertical lift foils generate helps significantly reduce the hydrodynamic resistance of the hull by raising it out of the water. Some craft, such as the IMOCA60 class, use foils for a hybrid purpose, combining these benefits. Craft that use foils for the latter purpose operate in two distinct regimes: hull-borne and foil-borne. The first occurs when the boat's speed is insufficient to generate enough lift to raise the hull out of the water, and the boat is supported by its buoyancy. When the boat passes through a threshold take-off speed, it becomes supported by its foils and enters the foiling regime (Acosta, 1973).

Foils used on race yachts face a large spectrum of hydrodynamic phenomena, since the boat speed varies greatly depending on wind speed, direction, and whether the boat is foiling or not. The operating regime encompasses lift

---

coefficients from zero up to near stall. Furthermore, the lift and drag forces are affected by the presence of the free surface. Typical Froude numbers for contemporary America's Cup yachts range from <1 to >10 depending on their speed. This range encompasses a shift in wave kinematics from subcritical to supercritical, as well as the possible onset of cavitation and natural ventilation at higher speeds(Acosta, 1973; Faltinsen, 2005). In parallel, the Reynolds numbers range from about 5×10^5 up to over 3×10^6 - hence appendage flows are often in the transitional regime. In addition, foil forces are highly sensitive to foil orientation, immersion, and interactions with other hull appendages (Oliver and Gauvain, 2022; Turnock and Holroyd, 2001). Such a wide operating regime makes it challenging for foil designers to carry out holistic hydrodynamic analyses of candidate foil designs. This kind of analysis is especially important for America's Cup teams due to the current generation of technical regulations, which restrict the degree of physical testing allowed for built foil prototypes.

Characterising the hydrodynamics of foils is typically done using computational tools with varying degrees of fidelity. Computational fluid dynamics (CFD), such as Reynolds-Averaged Navier–Stokes (RANS) formulations, are sought for their versatility and acceptable accuracy for a wide range of flows. They have seen extensive use in for yacht design (Turnock and Holroyd, 2001; Graf et al., 2009; Jones and Korpus, 2001). However, their drawback is high computational cost, especially for evaluating hundreds of candidate designs during conceptualisation. As a remedy, potential flow models such as panel methods (Giesing and Smith, 1967) or lifting line (LL) models can be used. These too are already widely used in naval architecture (Rosen and Laiosa, 1997; Oliver and Gauvain, 2022). They tend to be less accurate than CFD but offer improved computational efficiency.

The aim of this paper is to investigate two things: the discrepancies between RANS-based and LL-based simulation of simple hydrofoils; and the decomposition of drag forces acting on such hydrofoils within the framework of both modelling approaches. With the former, a numerical LL model is benchmarked against a RANS model of a fully submerged hydrofoil, followed by an analysis of different physical components of drag as a function of flow conditions. With this, the aim is to determine the usefulness of analysing drag decomposition with LL models during, for example, preliminary design. Such a decomposition could offer greater insight into the performance of a hydrofoil, since a designer could look to refine the design with a deeper understanding of how different drag mechanisms would be affected.

2 Implementation of CFD-based drag decomposition

A rectangular NACA4412 foil model with an aspect ratio of $\lambda = 6$ and chord of $c = 0.3$ m was used for simulations. No fillet radii were used at the wing tips. A geometric angle of attack of $\alpha = 5°$ was prescribed for all runs, with the foil's leading edge (LE) submerged one chord length beneath the undisturbed free surface. Figure 1 shows the domain dimensions and inlet/outlet boundary condition specifications.
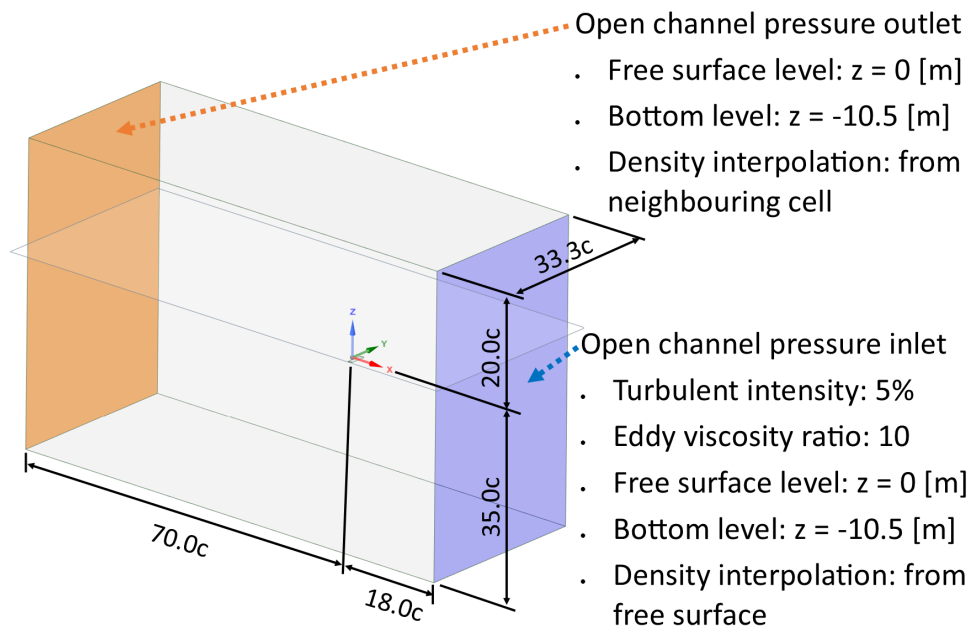

Figure 1: Computational domain used for simulations, with indicative dimensions and the inlet/outlet boundary conditions labelled. Detailed descriptions of the volume-of-fluid settings can be found in Inc. (2020).

The CFD implementation used to benchmark the lifting line (LL) results is described in Chernyshev et al. (2023a), and omitted here for conciseness. Flows were analysed at chord-based Froude numbers F_c of 0.5, 1, 2 and 4, which corresponded to inlet velocities of 0.858 ms^{-1}, 1.716 ms^{-1}, 3.431 ms^{-1} and 6.862 ms^{-1} respectively. The corresponding Reynolds numbers were 2.57×10^5, 5.15×10^5, 1.03×10^6 and 2.06×10^6.

The drag force, or resistance, experienced by foils moving through water has numerous physical sources. The most common way of extracting the drag force from CFD simulations is by integrating the normal and tangential stresses on the foil projected in the direction of motion (Hoerner, 1965). This way, components usually termed "pressure drag" and "skin friction drag" are obtained. Figure 2 depicts how further decompositions may be performed, along with the known ways of calculating each component. The methods used in this study were based on various forms of wake surveys that can calculate the wave, induced and viscous drag components. Their implementations are described in detail by Chernyshev et al. (2023b). Based on prior sensitivity analyses from the same reference, the wake plane location for the surveys was placed at 1.5 chord lengths downstream of the trailing edge. Due to the absence of any surface-piercing geometry in the present study, spray drag was not considered.
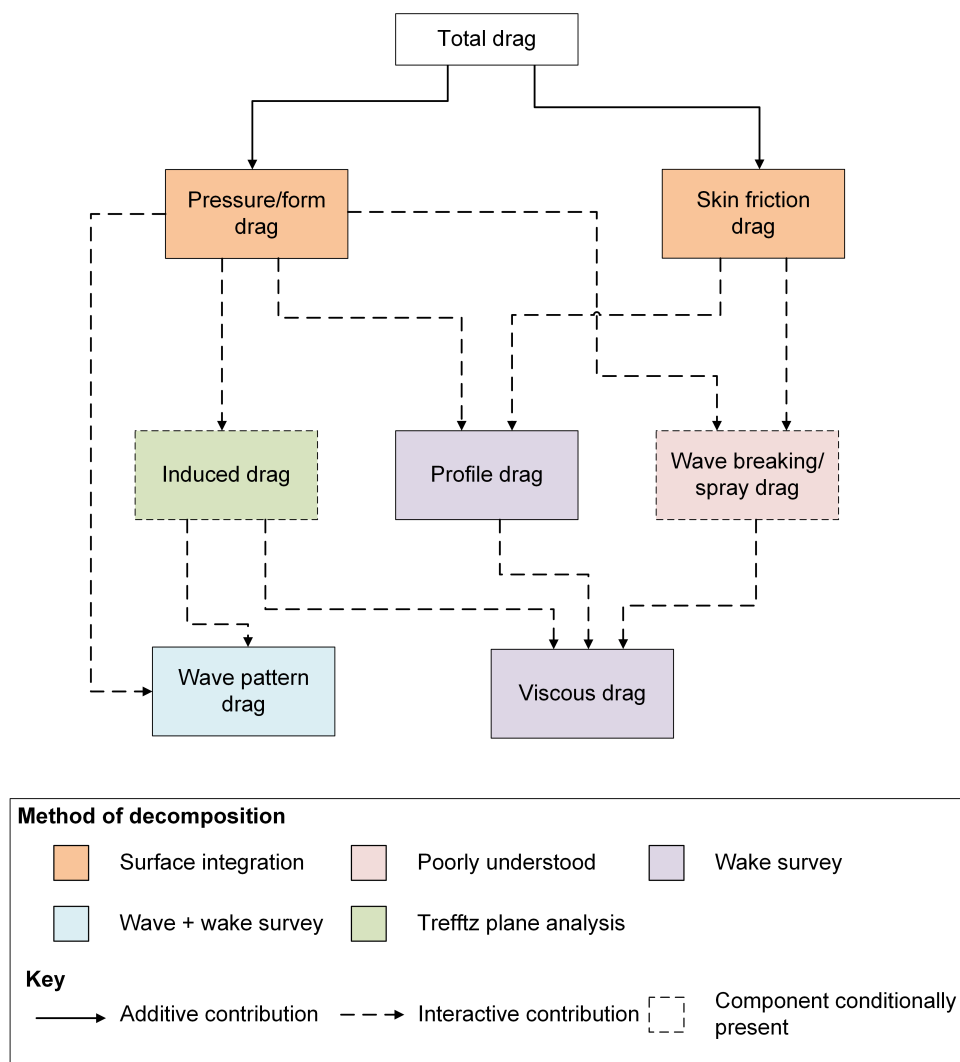

Figure 2: Hierarchical decomposition of drag forces on sailing yacht foils and appendages.

3   Methods - lifting line implementation

The lifting line model used in this paper is a numerical version of the analytical lifting line model of wings originally developed by Goates and Hunsaker (2019). This model is suitable for hydrofoils and airfoils with moderate to large aspect ratios - greater than about 4 - and small angles of attack where there is little to no flow separation. We used a package called "MachUpX" (Goates and Hunsaker, 2022), but modified it to account for the free surface effects present when simulating hydrofoils. The modified package, called "MachUpHydro" is available online (Chernyshev, 2023). The core of our method is largely the same as that presented by Goates and Hunsaker (2022), so most details will not be reproduced here. Instead, a description of the setup used for this

study is given in the following sections, alongside the key changes to some of the governing equations made to accommodate free surface effects. Unless otherwise specified, all other settings were default ones carried over directly from those suggested by Goates and Hunsaker (2022) based on their verification and sensitivity analyses.

3.1 Geometry and model settings

The simulated geometry was the same as that used in the CFD section above, except for the submergence h which was varied between $h/c = 0.25$ and $h/c = 4.00$. The input files used to specify this are shown in the appendix. The database used to compute the hydrofoil's section properties (lift, drag, moment) for each control point was pre-generated using XFOIL (Drela, 1989). This was implemented via the `airfoil-db` Python package. A separate database was generated for each Froude number simulated, ensuring a small buffer of $\pm 10\%$ above and below the nominal Reynolds number to account for variations due to the induced velocities at control points. Angles of attack between $-12°$ and $15°$, with a step of $0.1°$, were simulated for each Reynolds number. Because the nominal Mach number was negligible (less than 0.005 in the simulated water medium), the flow was treated as incompressible for all cases. Using interpolation, the lift, drag and moment coefficient were calculated for each segment of the lifting line at the effective angle of attack seen by that segment (in line with the practice of Goates and Hunsaker (2022)).

3.2 Modifications to account for free surface effects

A biplane image formulation was utilised, wherein the simulated hydrofoil is reflected about the mean free surface but with the bound and trailing vortices assumed rotating in the same sense as on the parent foil. Figure 3 illustrates this idea. Previous studies that used lifting line models for hydrofoils in the presence of a free surface deemed this formulation acceptable for accuracy (Nishiyama, 2013; Wu, 1953; Wilson, 1978; Morch and Minsaas, 1991; Walree, 1999).
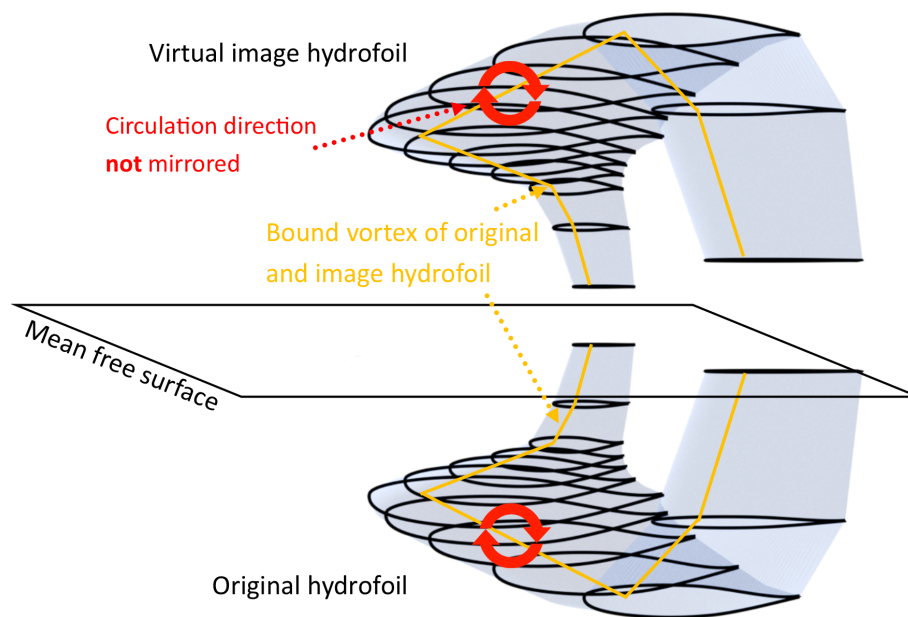

Figure 3: Illustration of biplane mirroring about the free surface to simulate interaction effects. The image was taken and modified from Kramer et al. (2018).

The biplane image was implemented by mirroring all of the vortex nodes about the mean free surface at $z = 0$ m. This was done using a standard vector mirror transform. The effect of this was to add additional terms to the expression of induced velocity v_{ji} at each control point. The original expression for v_{ji} is given as (eq. 36 in Goates

and Hunsaker (2022))

$$
\begin{aligned}
v_{ji} = \frac{1}{4\pi} \Bigg[& -\frac{\vec{u}_{\text{trailing}_j} \times \vec{r_0}}{r_0'(r_0' - \vec{u}_{\text{trailing}_j} \cdot \vec{r_0'})} + \frac{(r_0' + r_0)(\vec{r_0'} \times \vec{r_0})}{r_0' r_0 (r_0' r_0 + \vec{r_0'} \cdot \vec{r_0})} \\
& + (1 - \delta_{ij}) \frac{(r_0 + r_1)(\vec{r_0} \times \vec{r_1})}{r_0 r_1 (r_0 r_1 + \vec{r_0} \cdot \vec{r_1})} + \frac{(r_1' + r_1)(\vec{r_1'} \times \vec{r_1})}{r_1' r_1 (r_1' r_1 + \vec{r_1'} \cdot \vec{r_1})} \\
& + \frac{\vec{u}_{\text{trailing}_j} \times \vec{r_1'}}{r_1'(r_1' - \vec{u}_{\text{trailing}_{j+1}} \cdot \vec{r_1'})} \Bigg],
\end{aligned}
\tag{1}
$$

where $\vec{r_0}, \vec{r_1}, \vec{r_0'}$ and $\vec{r_1'}$ are the vector displacements between the ith control point and vortex node j and $j+1$, and vortex *joint* node j and $j+1$ respectively. The non-boldface variables represent magnitudes of the respective vectors. Trailing vortex direction vectors are denoted as $\vec{u}_{\text{trailing}_j}$ and $\vec{u}_{\text{trailing}_{j+1}}$ and δ_{ij} is the Kronecker delta function.

To calculate the induced velocities due to the mirrored lifting line, we would need to calculate new vector displacements to the mirrored vortex nodes and mirror the direction vectors of the trailing vortices. The former is done via

$$
\vec{r_{k,\text{image}}} = \vec{r_{\text{CP}}} - \vec{r_{\text{vortex,image}}},
\tag{2}
$$

where $\vec{r_{\text{vortex,image}}}$ is the mirrored counterpart of the jth and $j+1$th vortex node and $\vec{r_{\text{CP}}}$ is a given control point location from the *original* hydrofoil's lifting line locus. The subscript k is equal to either 0 or 1 depending on whether the jth or $j+1$th vortex node is being mirrored. To find the mirrored trailing vortex direction vectors, a simple vector mirroring operation was performed on the original vectors about the mean free surface.

With all the mirrored vectors now computed, the biplane correction to the induced velocities took the form

$$
v_{ji,\text{effective}} = v_{ji} \pm v_{ji,\text{image}}
\tag{3}
$$

where $v_{ji,\text{image}}$ is the same form as Equation (1) but using the mirrored counterparts of the displacement and direction vectors from the preceding calculations. The plus-minus sign is to be taken depending on whether the biplane or the wall boundary condition for the free surface was desired respectively.

3.3 *Modifications to account for wave-making*

In an effort to improve the fidelity of the lifting line model, wave-making effects were simulated in addition to the mean free surface effects described previously. This was done by adding the downwash produced due to the generation of the wave pattern by the hydrofoil using a method outlined by Morch (1992) based on free surface Green's functions – specifically Equation 2.3.1b and Appendix B. For brevity, the details of this calculation were not reproduced here. The resulting correction to the downwash coefficients from Equation (3) looked like

$$
v_{ji,\text{effective}} = v_{ji} \pm v_{ji,\text{image}} + v_{ji,\text{wave}},
\tag{4}
$$

where the last term of Equation (4) accounts for the effect of wave-making on the downwash coefficients.

4 Drag force decomposition from the lifting line model

Unlike for CFD, wake surveys cannot be used with lifting line solutions directly, due to the lack of a resolved wake flow field in the calculation. Instead, a simple separation of the downwash components, as per Equation (4), was used in combination with the Kutta-Zhukovsky theorem to calculate the inviscid – wave and induced – resistance components. The viscous component was calculated using the 2D viscous XFOIL simulations of each segment.

In MachUpHydro, the viscous drag force F_{Dv} was calculated as the sum of the discrete wing segment drag forces. For each segment, the local drag coefficient was computed by interpolating into the hydrofoil database created by XFOIL at the effective angle of attack (as defined in Section IV B of Goates and Hunsaker (2022)) and effective Reynolds number seen by that segment. After thus determining the total viscous drag force on the hydrofoil, the viscous drag coefficient was computed through

$$
C_{Dv} = \frac{2F_{Dv}}{\rho V_\infty^2 S}
\tag{5}
$$

where S is the planform area.

Assuming zero coupling between the induced and viscous drag components, the former could simply be calculated as the component of the total inviscid force acting in the freestream direction. In the numerical lifting line model, the inviscid force was calculated by applying the Kutta-Zhukovsky theorem to each discretised wing segment using

$$\Delta \vec{F}_{\Gamma_i} = \rho \Gamma_i \vec{V}_i \times \vec{dl}_i; \tag{6}$$

where $\Delta \vec{F}_{\Gamma_i}$ is the inviscid force vector acting on segment i; Γ_i is the segment's circulation; V_i is the total velocity vector at the segment's control point $\vec{V}_i = \frac{\Gamma_i}{4\pi} v_{ji}$, and $\vec{dl}_i$ is the bound vortex vector for that segment. Therefore, taking the component of this force acting in the freestream direction yields the inviscid drag $D_{\text{inviscid},i}$ acting on segment i,

$$D_{\text{inviscid},i} = \Delta \vec{F}_{\Gamma_i} \cdot \vec{u}_\infty. \tag{7}$$

The total inviscid drag acting on the hydrofoil is then the sum of $D_{\text{inviscid},i}$ from each segment. To decompose this further, it is necessary to assume that induced and wave drag are coupled with each other through the effect of the mean free surface via the biplane image formulation (judged to be a fair assumption based on prior studies (Chernyshev et al., 2023a)). Then the inviscid force from Equation (6) can be decomposed by breaking down $\vec{V}_i$ into three parts: self-induced downwash $\vec{V}_{si}$; downwash induced by the biplane image of the foil $\vec{V}_{bi}$; and downwash due to the wave-making correction $\vec{V}_{wi}$. Consequently, the inviscid force due to wave-making is derived from Equation (6) as

$$\Delta \vec{F}_{\Gamma_i} = \rho \Gamma_i (\vec{V}_{wi} + \vec{V}_{bi}) \times \vec{dl}_i; \tag{8}$$

and the force due to lift-induced effects is

$$\Delta \vec{F}_{\Gamma_i} = \rho \Gamma_i (\vec{V}_{si} + \vec{V}_{bi}) \times \vec{dl}_i. \tag{9}$$

Note the inclusion of the induced drag due to the biplane image in both Equation (8) and Equation (9). While it is not obvious how the wave drag and induced drag mechanisms interact, it is safe to assume that the biplane image influences both. For wave drag, this is because the biplane image approximates the effects of free surface's proximity, and the wave corrections of Equation (4) can be considered a subset of this. Meanwhile, the induced drag depends on the lift, which itself is altered by the presence of the free surface due to the downwash from the biplane image. Hence the biplane image factors into both components of inviscid drag.

After calculating the drag forces per Equations (8) and (9), the corresponding drag coefficient was found in a manner analogous to Equation (5).

5 Results and discussion

To ascertain the validity of the CFD simulations, in Figure 4 we examined whether, as suggested by the Froude hypothesis, the viscous and wave drag components sum to the total drag (Wu, 1962). Here, the sum of the viscous and wave drag coefficients is plotted alongside the total drag coefficient extracted directly from CFD via surface integration. The sum was remarkably close to the total at all simulated Froude numbers, which supported the Froude hypothesis. Figure 4 also shows that the strong decrease in the wave drag coefficient with Froude number led to an overall decline of the total drag coefficient. Likewise, the "hump" in C_{Dw} around $F_c = 1$ was reflected with a hump in $C_{D,\text{tot}}$ at the same location. This demonstrated that in the intermediate Froude number regime $0.5 < F_c < 2$ wave drag constituted a significant, if not dominant, part of the foil's overall drag.
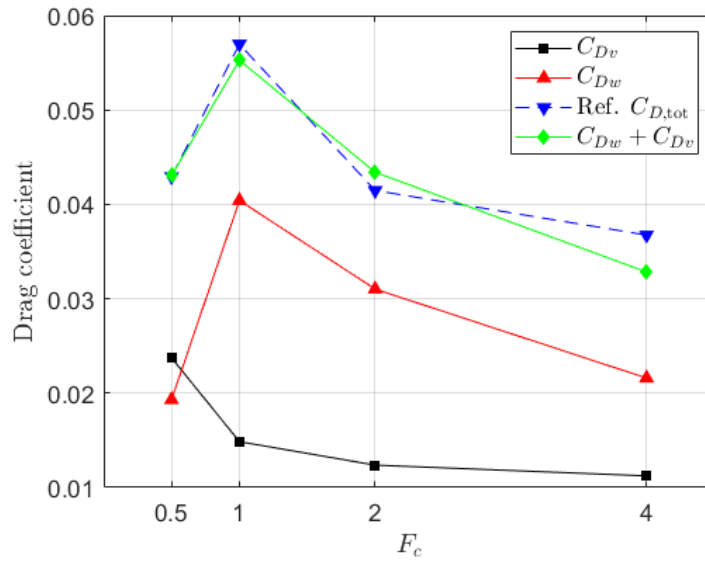
Figure 4: Examining the validity of the CFD drag decomposition through the Froude hypothesis.

5.1 Benchmarking lifting line calculations against CFD

Next, lifting line simulations were performed with the same geometry and conditions as for CFD. Figure 5 plots the total drag coefficients from both methods as function of the simulated Froude number. The overall trend from CFD was captured well by the LL model, with the drag sharply increasing up to a peak around $F_c = 1$ before slowly decreasing as F_c increased. However, the magnitude of the peak drag coefficient was underestimated by the LL model compared to CFD. This could be explained by strong non-linearities in the free surface wave pattern that were not accurately modelled by the wave-making correction applied to the LL model. Conversely, at $F_c \gtrsim 2$, the LL model started overestimating the total drag, perhaps again due to differences between the theoretical (LL) and resolved (CFD) free surface deformations.
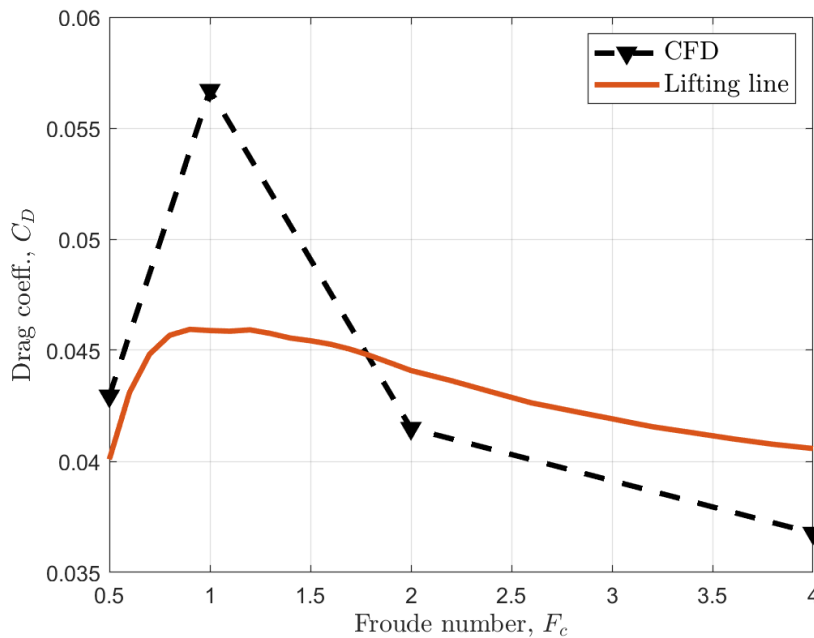

Figure 5: Calculated total drag coefficients with $\lambda = 6$, $h/c = 1$ and $\alpha = 5°$ using CFD and lifting line.

The viscous drag coefficient C_{Dv} was calculated for all simulated Froude numbers and is shown in Figure 6. Results are presented alongside the C_{Dv} from RANS CFD simulations. The main point to note here is that C_{Dv} from CFD was underestimated by the LL model at all simulated Froude numbers, by about half. This result showed that

perhaps the induced velocities at the control points of the LL were not modelled very accurately. Most likely, the reason was that the XFOIL panel method used to calculate the section drag coefficient used rather rudimentary viscous flow models which did not account for additional viscous effects that were simulated in RANS – namely boundary layer growth and transition. These would have resulted in a greater pressure drag on each segment of the discretized wing, and increased the effective angle of attack seen by each control point.
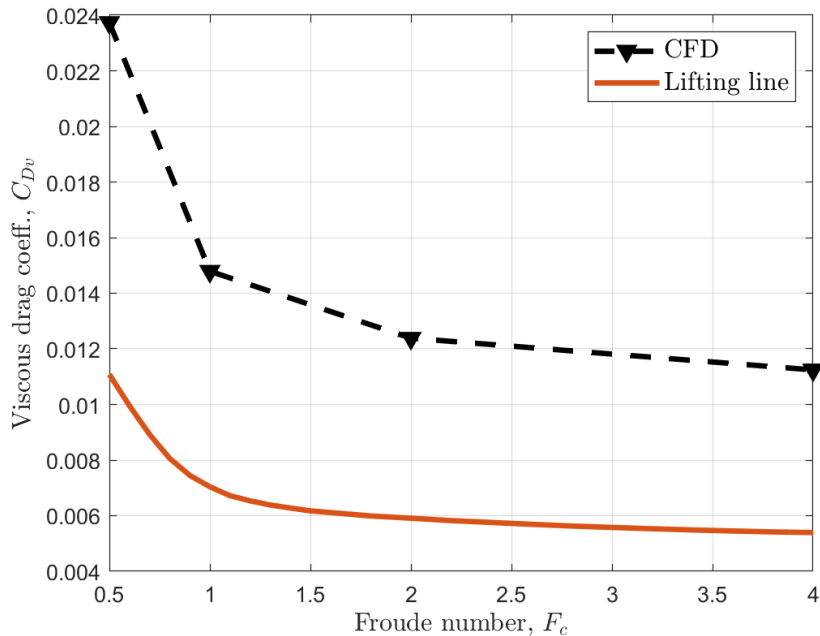

Figure 6: Calculated viscous drag coefficients with $\lambda = 6$, $h/c = 1$ and $\alpha = 5°$ using CFD and lifting line.

A comparison of the induced drag coefficient C_{Di} from CFD and LL is shown in Figure 7. At $F_c > 1$, the CFD model showed that C_{Di} approached a plateau of around 0.028 as F_c increased. The LL model was able to capture this trend reasonably well, though it appeared that the LL values of C_{Di} were still increasing at the highest simulated Froude number, suggesting the plateau point would be at higher Froude numbers than what were simulated here.

At $F_c = 0.5$, the LL model did not agree with CFD. While the LL model predicted a monotonically increasing induced drag coefficient through the whole range of simulated Froude numbers, the CFD simulations suggested the induced drag encountered a local minimum around $F_c = 1$ – granted, the resolution of Froude numbers in this area should be improved to elucidate this trend. This could be attributed to either an interaction with the free surface that changed the lift such as to reduce C_{Di}; or an inaccuracy with the wake survey. Through a previous sensitivity analysis (Chernyshev et al., 2023b), it was found that at $F_c < 1$ wake surveys were quite sensitive to the choice of downstream position for the wake plane. For consistency, the same position was used for all Froude numbers in the present CFD simulations, but for future studies perhaps the choice should depend on the Froude number to reflect the different nature of the wakes.
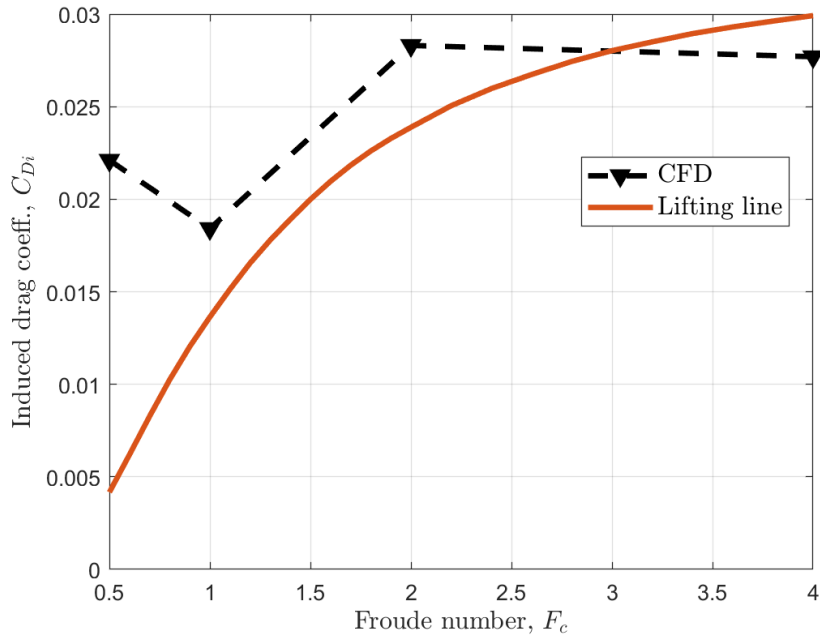
Figure 7: Calculated induced drag coefficients with $\lambda = 6$, $h/c = 1$ and $\alpha = 5°$ using CFD and lifting line.

Figure 8 shows a comparison between the wave drag coefficient C_{Dw} computed from the LL model and from CFD. In both cases, there was a "hump" in C_{Dw} at a certain F_c. In the CFD model, it occurred around $F_c = 1$ with a peak of 0.040; whereas in the LL model it was at about $F_c = 0.75$ with a peak of 0.028. Both cases reflected the approximate flow regime where wave drag is maximised due to the nature of the wave pattern on the free surface Wehausen (1973). After the hump, the wave drag was expected to gradually decrease as the Froude number went up, but to not reach zero. This is because in the high Froude number regimes, about $F_c > 2$, the transverse waves start to disappear and the only significant contribution to the wave drag comes from the diverging wave system (Nishiyama, 2013). This trend was seen in both models, with the wave drag from each steadily declining after the hump. However, there was still a large discrepancy between the predicted values due to the difference in peak C_{Dw} at the humps. This could be due to wave pattern structures that were resolved explicitly by the CFD model using a volume-of-fluid (VOF) model while only being theoretically modelled using the wave correction term of Equation (4) in the LL model. Addressing this would probably require a higher-fidelity theory for performing the wave correction.
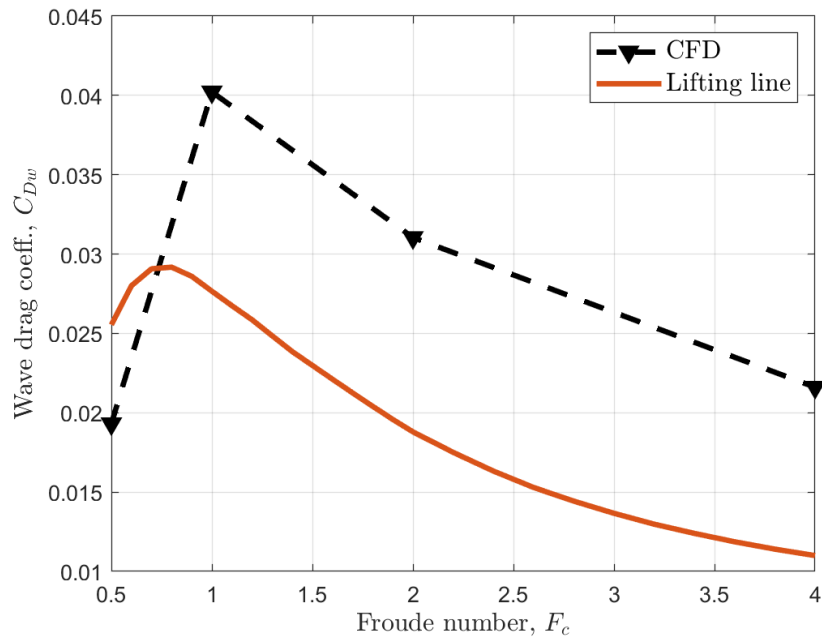
Figure 8: Calculated wave drag coefficients with $\lambda = 6$, $h/c = 1$ and $\alpha = 5°$ using CFD and lifting line.

5.2 *Examining the influence of submergence depth on drag components*

The submergence depth of a foil is known to drastically influence its hydrodynamics (Vladimirov, 1955). In this section, the submergence-dependence of the viscous, induced and wave drag components is examined using the LL model.

Figure 9 shows the total drag coefficient for submergence depths between $h/c = 0.25$ and $h/c = 4.00$ and F_c between 0.5 and 4. A strong submergence influence was evident. At the shallowest submergence, the total drag increased with Froude number up to a peak around $F_c = 1.75$, before slowly declining again. Also, as the submergence increased, the location of peak total drag coefficient shifted to lower Froude numbers and higher values. Such a peak was seen at all submergences except for the deepest ones of 3.00 and 4.00 chords. At these depths, the C_D was greatest at the lowest simulated Froude number, after which it monotonically decreased with F_c. Perhaps expanding the lower range of Froude numbers to around 0.25 would also reveal a peak in C_D for the greatest submergences.

It can also be observed in Figure 9 that the total drag at $F_c = 0.5$ increased as the submergence increased. This meant the total drag at lower Froude numbers was lower when the submergence was shallower. Looking to the highest Froude numbers, it was seen that the total drag attained at intermediate submergences was greater than that at the lowest of the highest ones. The result at the shallowest submergence, $h/c = 0.25$, should be treated with caution though. At the intermediate and high Froude number regimes, strong interactions between the free surface and suction side of the foil could result in the onset of ventilation which cannot be explicitly resolved or accurately modelled by the LL method, unless utilising an empirical correction.
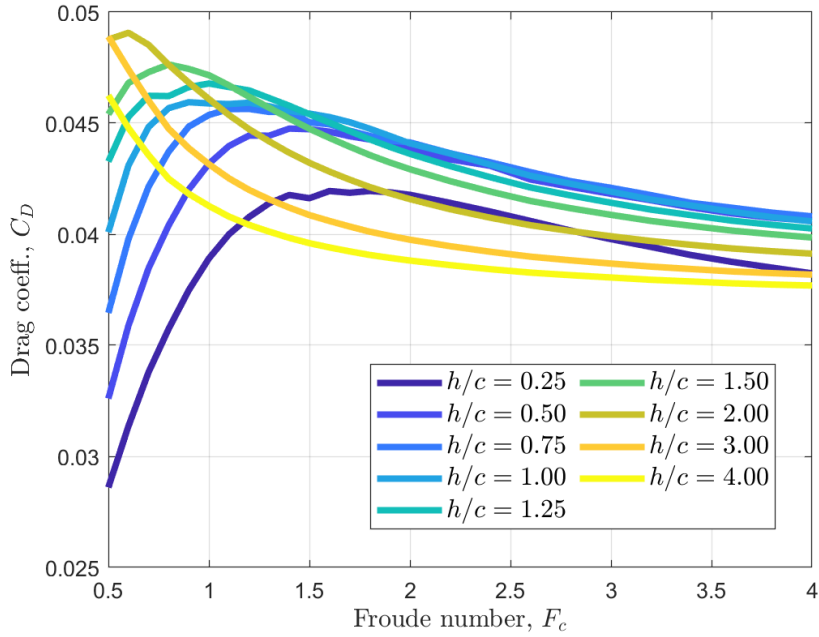
Figure 9: Calculated total drag coefficients with $\lambda = 6$ and $\alpha = 5°$ at different LE submergences.

Further insight into the trends seen in the total drag coefficient can be obtained through drag decomposition. In Figure 10, the viscous component is presented as a function of submergence and Froude number. It appeared that submergence did not greatly influence C_{Dv} except for at the lowest simulated Froude numbers, $F_c < 0.75$. In this regime, the viscous drag was greatest at the shallowest submergences by around 33%. On the contrary, at the highest Froude numbers the viscous drag was greater the higher the submergence, with around 10% separating the drag at the highest submergence from that at the lowest one. In general, the viscous drag component decreased with Froude number because of the accompanying boundary layer transition at higher Reynolds numbers.
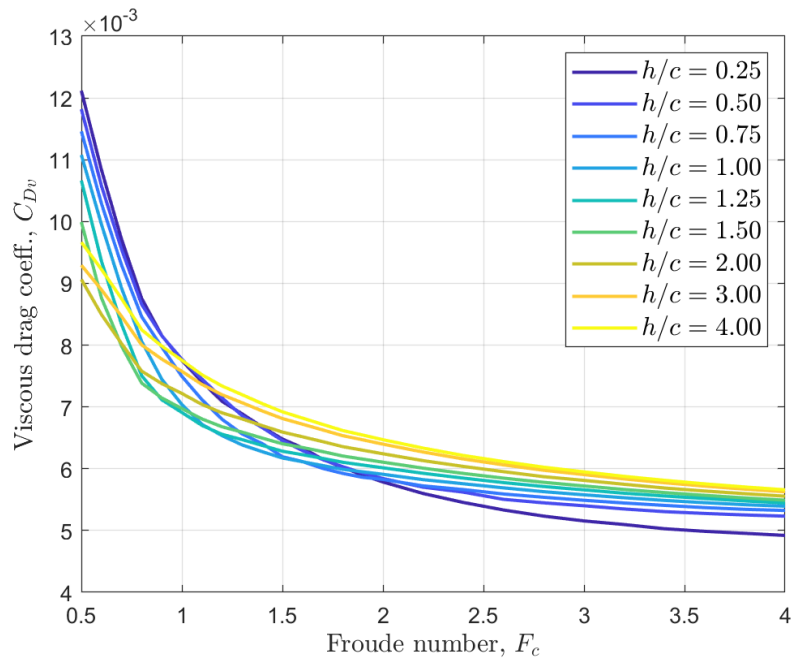

Figure 10: Calculated viscous drag coefficients with $\lambda = 6$ and $\alpha = 5°$ at different LE submergences.

The induced drag coefficient C_{Di} is shown in Figure 11 for all simulated submergences and Froude numbers. It appeared that generally C_{Di} increased as the submergence increased, across all Froude numbers that were sim-

ulated. This was likely because these simulations were done with a constant angle of attack, instead of a constant lift. Because of this, the lift at shallower submergences was affected by the proximity of the free surface.

At shallower submergences, the induced drag increased more gradually as the Froude number went up. For example, at $h/c = 0.25$, C_{Di} increased from about 0.0025 to 0.025 over the whole range of Froude numbers – a 900% increase. By contrast, at the highest submergence, C_{Di} increased from 0.025 to only 0.032, which was a 28% increase. Furthermore, at this submergence C_{Di} attained a relatively constant value past a Froude number of around two, whereas at shallower submergence such a plateau was not observed. This showcased the significance of free surface effects on the induced drag coefficients across all Froude number regimes.
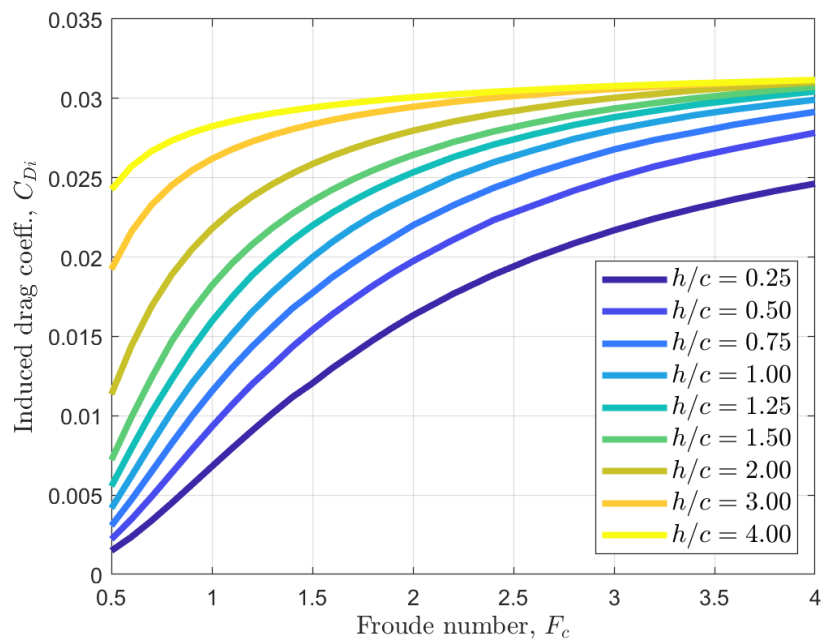

Figure 11: Calculated induced drag coefficients with $\lambda = 6$ and $\alpha = 5°$ at different LE submergences.

Finally, the wave drag coefficient C_{Dw} is displayed in Figure 12. Here, the cause of the peaks in the total drag coefficient seen in Figure 9 is revealed, with C_{Dw} exhibiting similar peaks at intermediate Froude numbers. These shifted up and to the left on the plot as the submergence was increased. At a given submergence, the wave drag trended to a somewhat asymptotic value at high Froude numbers. This value decreased the greater the submergence was. This trend can be explained by the fact that wave drag depends on the free surface wave pattern generated by the foil's pressure disturbance. The closer the foil is to the free surface, the stronger its interaction with it becomes; hence the wave drag acting on the foil increases (Acosta, 1973). Hence the wave drag coefficient tended to be greater at shallower submergences.

Exceptions to this can be seen, however, at the lower Froude numbers. For example, at around $F_c \lessgtr 0.75$, the wave drag coefficient at $h/c = 2.00$ exceeded that at $h/c = 0.25$ despite the latter being at a shallower submergence. Other similar cross-over points can be observed for the other simulated submergences as well. As before, this was probably due to the nature of the wave correction formulation used and the corresponding physical implications – i.e. that the wave-induced downwash strongly depended on both Froude number and submergence. It would be desirable to perform another set of CFD simulations at a different submergence to see if these trends would be reflected in the higher-fidelity results.

Two distinct regimes could be seen in Figure 12 – one below the peak C_{Dw} and one beyond it. The drop in C_{Dw} as the Froude number decreased below the peak location was steeper than that when the Froude number increased past it. This reflected the shifting in the dominant source of wave drag from transverse to diverging waves.

These results are an example of one of endless parameter studies marine architects and naval engineers could employ to study the hydrodynamics of their proposed foil designs in great detail during the preliminary conception. However, care should be taken with interpretation of the results, as much of the numerical LL modelling relies on theoretical corrections that can be difficult to validate. For this reason, more detailed design analysis should be performed with a higher-fidelity approach such as CFD due to greater reliability of the results.
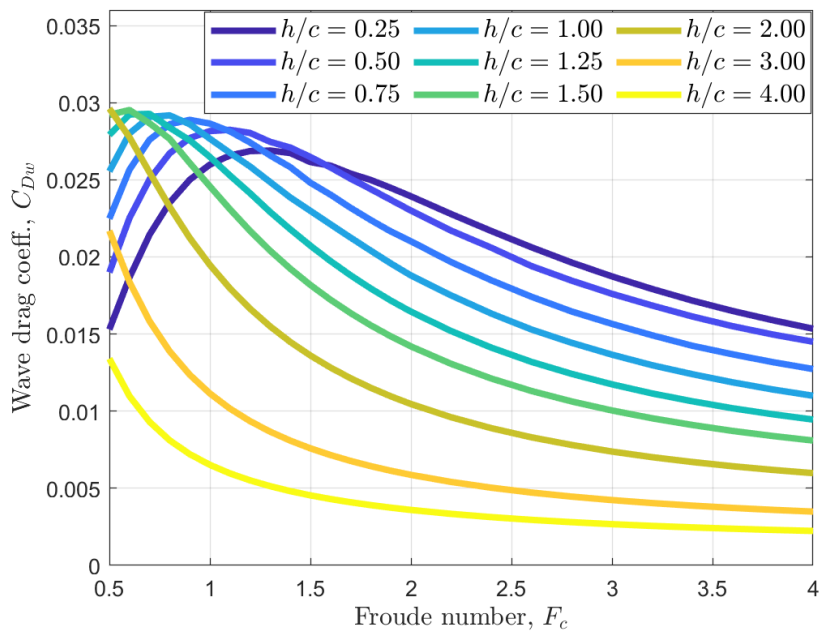
Figure 12: Calculated wave drag coefficients with $\lambda = 6$ and $\alpha = 5°$ at different LE submergences.

6   Conclusions and further research

A NACA4412 rectangular hydrofoil was simulated in a fully submerged configuration moving at a constant Froude number using both RANS-based CFD and a numerical LL model. Decompositions of the drag force acting on the hydrofoil were performed. From CFD, it was possible to extract the induced, viscous and wave drag components using various wake survey methods. Comparing the total drag force with the sum of viscous and wave drags yielded excellent agreement, supporting the widely accepted Froude decomposition of hydrodynamic drag.

The same drag coefficients were also computed from the numerical LL model. Significant discrepancies were seen when compared to the CFD model, but mostly those that would be reasonably expected due to the differing nature in which both methods function and their corresponding fidelity to real free surface flows. Otherwise, the trends were reflected in the LL model adequately. Building on this, a study of the effect of submergence depth of the hydrofoil was carried out. Strong submergence-dependence of the induced and wave drag components was observed. Higher submergences led to overall lower total drag except at Froude numbers below around 1.5. In this intermediate regime, strong wave effects acted to increase the total drag compared to even shallower submergences. It would be desirable to perform more high-fidelity CFD simulations at different submergences along with the corresponding drag force decompositions, to benchmark the trends predicted by the more simplified LL model. This would clarify the accuracy of these trends and whether they properly reflect the effect of waves and submergence on the hydrofoil's drag components.

The efficiency of the numerical LL model here, demonstrated through an extensive parameter study on submergence depth, can be greatly exploited for exploring a large design space to optimise candidate designs during preliminary conception. However, great care should be taken in interpreting these results as the theoretical models employed, especially for the free surface effects, can be difficult to validate and still shows significant discrepancies with CFD.

Acknowledgements

References

Acosta, A., 1973. Hydrofoils and hydrofoil craft. Annual Rev. Fluid Mechanics 5, 161–184.

Chernyshev, L., 2023. Machuphydro.

Chernyshev, L., Kabaliuk, N., Jermy, M., Corkery, S., Bernasconi, D., 2023a. Determining the physical components of resistance acting on a hydrofoil. doi:10.1115/IMECE2023-112475.

Chernyshev, L., Kabaliuk, N., Jermy, M., Corkery, S., Bernasconi, D., 2023b. Developing methods of decomposing the physical resistance components acting on a hydrofoil. IOP Conf. Series: Materials Sci. Eng. 1288, 012038. doi:`10.1088/1757-899X/1288/1/012038`.

Drela, M., 1989. Xfoil: An analysis and design system for low reynolds number airfoils, in: Mueller, T.J. (Ed.), Low Reynolds Number Aerodynamics, Springer Berlin Heidelberg. pp. 1–12.

Faltinsen, O.M., 2005. Hydrodynamics of high-speed marine vehicles. Cambridge university press.

Giesing, J.P., Smith, A., 1967. Potential flow about two-dimensional hydrofoils. J. Fluid Mechanics 28, 113–129.

Goates, C., Hunsaker, D., 2019. Airfoil database documentation.

Goates, C.D., Hunsaker, D.F., 2022. Modern implementation and evaluation of lifting-line theory for complex geometries. J. Aircraft 60, 490–508. doi:`10.2514/1.C036748`.

Graf, K., Boehm, C., Renzsch, H., 2009. Cfd- and vpp-challenges in the design of the new ac90 americas cup yacht, in: SNAME 19th Chesapeake Sailing Yacht Symp., p. D011S001R001. doi:`10.5957/CSYS-2009-001`.

Hoerner, S.F., 1965. Fluid-dynamic drag. Hoerner fluid dynamics.

Inc., A., 2020. ANSYS Fluent Theory Guide. Report.

Jones, P., Korpus, R., 2001. International america's cup class yacht design using viscous flow cfd, in: SNAME 15th Chesapeake Sailing Yacht Symp., p. D011S001R004. doi:`10.5957/CSYS-2001-004`.

Kramer, J.V., Godø, J.M.K., Steen, S., 2018. Hydrofoil simulations–non-linear lifting line vs cfd, in: Numerical Towing Tank Symp.

Morch, J.B., 1992. Aspects of Hydrofoil Design; With Emphasis on Hydrofoil Interaction in Calm Water. Thesis.

Morch, J.B., Minsaas, K.J., 1991. Aspects of hydrofoil design; with emphasis on hydrofoil interaction in calm water.

Nishiyama, T., 2013. Linearized steady theory of fully wetted hydrofoils. Advances Hydroscience 3, 237–342.

Oliver, C., Gauvain, E., 2022. Practical performance prediction of foil-configured monohull yachts, in: SNAME 24th Chesapeake Sailing Yacht Symp., OnePetro.

Rosen, B.S., Laiosa, J.P., 1997. Splash nonlinear and unsteady free-surface analysis code for grand prix yacht design, in: SNAME 13th Chesapeake Sailing Yacht Symp., OnePetro.

Turnock, S.R., Holroyd, N.J., 2001. Appendage design for the america's cup using cfd, in: European Congr. on Comput. Methods in Appl. Sci. and Eng.

Vladimirov, A., 1955. Approximate hydrodynamic design of a finite span hydrofoil. Report. Central Aero-Hydrodynamical Institute.

Walree, F.V., 1999. Computational methods for hydrofoil craft in steady and unsteady flow. Thesis.

Wehausen, J.V., 1973. The wave resistance of ships. Advances Appl. Mechanics 13, 93–245.

Wilson, M.B., 1978. Lifting Line Calculations for Hydrofoil Performance at Arbitrary Froude Number and Submergence. Part 1. Fixed Shape Elliptical Circulation Distribution. Report. D. W. Taylor Naval Ship Research and Development Center.

Wu, J., 1962. Separation of viscous from wave-making drag ship forms. J. Ship Res. 6.

Wu, Y., 1953. A theory for hydrofoils of finite span. Report. California Institute of Technology Hydrodynamics Lab.